Rapid fabrication of MgO@g-C$_3$N$_4$ heterojunctions for photocatalytic nitric oxide removal

Minh-Thuan Pham[1,2,3], Duyen P. H. Tran[1,2,3], Xuan-Thanh Bui[4] and Sheng-Jie You[*2,3]

Full Research Paper

`Open Access`

Address:
[1]Department of Civil Engineering, Chung Yuan Christian University, Taoyuan 32023, Taiwan, [2]Department of Environmental Engineering, Chung Yuan Christian University, Taoyuan 32023, Taiwan, [3]Center for Environmental Risk Management, Chung Yuan Christian University, Taoyuan 32023, Taiwan and [4]Faculty of Environment and Natural Resources, Ho Chi Minh City University of Technology (HCMUT), VNU-HCM, 268 Ly Thuong Kiet Street, District 10, Ho Chi Minh City 700000, Viet Nam

Email:
Sheng-Jie You[*] - sjyou@cycu.edu.tw

* Corresponding author

Keywords:
g-C$_3$N$_4$; MgO; nitric oxide; photocatalyst; visible light

Abstract

Nitric oxide (NO) is an air pollutant impacting the environment, human health, and other biotas. Among the technologies to treat NO pollution, photocatalytic oxidation under visible light is considered an effective means. This study describes photocatalytic oxidation to degrade NO under visible light with the support of a photocatalyst. MgO@g-C$_3$N$_4$ heterojunction photocatalysts were synthesized by one-step pyrolysis of MgO and urea at 550 °C for two hours. The photocatalytic NO removal efficiency of the MgO@g-C$_3$N$_4$ heterojunctions was significantly improved and reached a maximum value of 75.4% under visible light irradiation. Differential reflectance spectroscopy (DRS) was used to determine the optical properties and bandgap energies of the material. The bandgap of the material decreases with increasing amounts of MgO. The photoluminescence spectra indicate that the recombination of electron–hole pairs is hindered by doping MgO onto g-C$_3$N$_4$. Also, NO conversion, DeNOx index, apparent quantum efficiency, trapping tests, and electron spin resonance measurements were carried out to understand the photocatalytic mechanism of the materials. The high reusability of the MgO@g-C$_3$N$_4$ heterojunction was shown by a five-cycle recycling test. This study provides a simple way to synthesize photocatalytic heterojunction materials with high reusability and the potential of heterojunction photocatalysts in the field of environmental remediation.

Introduction

The rapid development of industrialization has been continuously increasing the combustion of fossil fuels, which leads to a large extent of nitrogen oxide emissions. This particular type of air pollutant leads to environmental damage (e.g., smog and acid) and health problems (e.g., COPD and cardiovascular diseases) [1-3]. Presently, there are different approaches to miti-

gate NO pollution, including catalyst/non-catalyst [4], oxidation [5], bioprocesses [6], adsorption [7], absorption [8], and non-thermal plasma technologies [9]. Photocatalytic oxidation is considered a promising approach due to its ability to degrade various air pollutants with light under ambient conditions [10].

Due to its unique properties, such as high chemical stability and low synthesis cost, graphitic carbon nitride has attracted considerable attention in the realm of environmental remediation [11-13]. It is an organic semiconductor that effectively absorbs visible light due to its small bandgap below 2.7 eV. Because of this, it has been consistently regarded as a catalyst with excellent optical properties [14,15]. Unfortunately, its narrow bandgap leads to rapid recombination of electron–hole (e^-–h^+) pairs, and the valence band potential of g-C_3N_4 (+1.75 eV) is more negative than that of H_2O/•OH (+2.40 eV), reducing the photocatalytic efficiency [16,17]. A well-known approach for overcoming this problem in order to achieve increased photocatalytic performance is to couple two semiconductors with optimal band alignment.

MgO is an alkaline metal oxide with wide bandgap (3.5–5 eV), high availability, non-toxicity, low cost, and native structural defects [18,19]. The large bandgap energy is the limitation of MgO, reducing the photocatalytic performance and applicability of MgO [20]. Various efforts have been made to enhance the absorption in the visible light region, including nonmetal and noble-metal doping, metal deposition, and formation of heterojunctions [21,22]. The construction of heterojunction structures has shown its effectiveness in improving photocatalytic performance by enhancing the separation of charge carriers and optimizing the redox potential by coupling two or more semiconductors [23,24], such as Bi_2MoO_6-based [25-29], BiOCl-based [30,31], g-C_3N_4-based [32-34], ZnO-based [35-37], TiO_2-based [38,39], and MgO-based heterostructured photocatalysts [40]. Among these, the combination of MgO and g-C_3N_4 with a lower bandgap is an efficient process for improving the photocatalytic performance. Li and co-workers reported an improvement in the photocatalytic efficiency of MgO@g-C_3N_4 for the photoreduction of CO_2 under visible light [33]. Similarly, MgO-modified g-C_3N_4 nanostructures enhanced the removal efficiency for NO_x, NO, and NO_2 [12]. However, these studies only focused on the synthesis of MgO from $Mg(NO_3)_2 \cdot 6H_2O$, increasing time and cost of the synthesis process. Commercial MgO as a precursor material for MgO@g-C_3N_4 heterojunctions has not been studied. Furthermore, there are no relevant reports on the fabrication of the MgO@g-C_3N_4 heterojunction via one-step pyrolysis nor on the photocatalytic pathway of the MgO@g-C_3N_4 heterojunction for photocatalytic NO removal under visible light.

In this study, a MgO@g-C_3N_4 heterojunction was synthesized via a one-step pyrolysis method using commercial MgO and urea and, subsequently, characterized. Charge transfer dynamics in the heterojunction and band structure were investigated to understand the effect of the heterojunction on the photocatalytic activity. Finally, the photocatalytic pathway of the MgO@g-C_3N_4 heterojunction was studied via trapping test, electron spin resonance (ESR) measurements, and other methods. This work might be helpful for the development of MgO@g-C_3N_4 heterojunction materials.

Experimental
Synthesis of MgO/g-C_3N_4
For the synthesis of g-C_3N_4, 30 g of urea was ground manually for 30 min and then placed in a 100 mL crucible. Then, the sample was annealed at 550 °C for two hours and let to cool to room temperature.
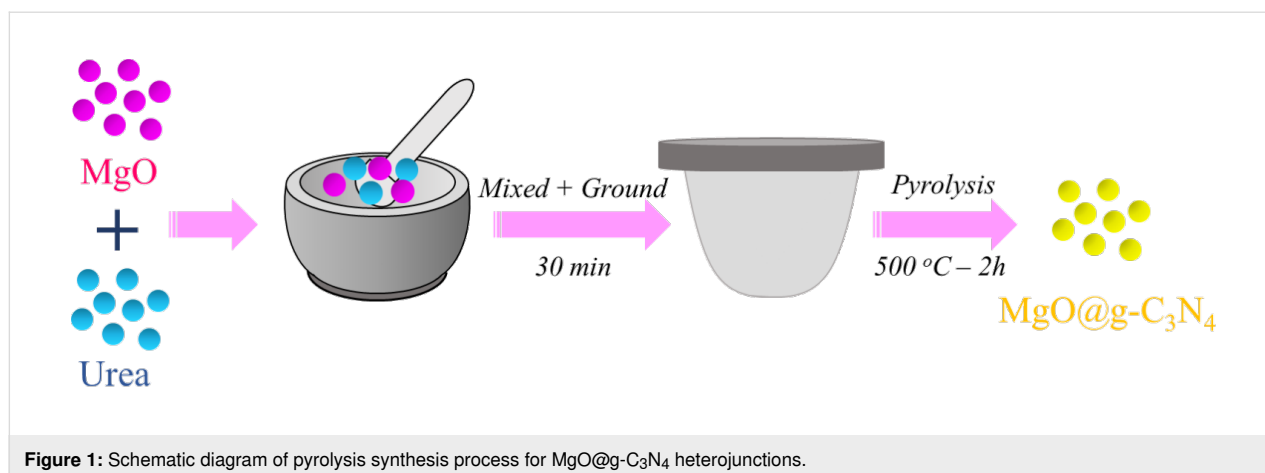
For preparation of the MgO@g-C_3N_4 heterojunction material, both MgO and urea were mixed, ground, and placed in a 100 mL crucible, followed by annealing at 550 °C for two hours (Figure 1). Then, the samples were let to cool to room temperature naturally. Different mass ratios of MgO and g-C_3N_4 were prepared, that is, 1%, 3% and 5%, named as x-MgO@g-C_3N_4 (x = 1, 3, and 5%).

Characterization
A variety of analytical techniques have been employed to evaluate the morphology and the physical, chemical, and optical properties of the materials. Scanning electron microscopy (SEM) and high-resolution transmission electron microscopy (HR-TEM) were used to assess the morphology of the materials. The crystal phase of the materials was determined by X-ray diffraction (XRD) with a measurement range of 10°–80°. Fourier-transform infrared spectroscopy (FTIR) was used to determine the chemical bond composition of the materials. Differential reflectance spectroscopy (DRS) determined the change in the bandgap of the materials. The elements of the materials were identified by high-resolution X-ray photoelectron spectroscopy (HR-XPS). The photoluminescence (PL) spectra of the materials was carried out in the form of fluorescence analysis with an excitation wavelength range of 200–900 nm. Finally, the photocatalytic mechanism was determined by trapping tests and ESR measurements.

Photocatalytic performance
The photocatalytic activity of as-prepared MgO@g-C_3N_4 was evaluated by monitoring NO degradation. The photocatalytic NO removal experiments were performed using a 4.5 L reaction chamber and a Xenon lamp (300 W) as the visible light source. The initial NO concentration was 500 ppb, the flow rate

Figure 1: Schematic diagram of pyrolysis synthesis process for MgO@g-C$_3$N$_4$ heterojunctions.

was 1.5 L·min^{-1}, and the dosage of catalysts was 0.2 g for all experiments. Before each catalytic experiment, 0.2 g of the sample was dispersed in 10 mL of DI water, evaporated at 80 °C, and placed in the dark to achieve adsorption–desorption equilibrium. Finally, the sample was illuminated by a Xenon lamp (300 W) for 30 min.

Trapping experiments were performed to evaluate the photocatalytic process mechanism for NO degradation. Three trapping agents were used representing different active species, namely isopropyl alcohol (IPA) for the hydroxyl radical (•OH), potassium dichromate (K$_2$Cr$_2$O$_7$) for electrons (e$^-$), and potassium iodide (KI) for holes (h$^+$). The photocatalytic NO degradation experiments were performed under the previously described conditions.

The photocatalytic NO degradation efficiency (η), the yield of NO$_2$ conversion (γ), the apparent quantum efficiency (AQE, φ), and the DeNOx index (αDeNOX αDeNOx) were calculated by using Equations 1–4: [41-43]:

$$\eta = \frac{C_{NO,\,i} - C_{NO,\,f}}{C_{NO,\,i}} \cdot 100\%, \tag{1}$$

$$\gamma = \frac{C_{NO_2,\,f} - C_{NO_2,\,i}}{C_{NO,\,i} - C_{NO,\,f}} \cdot 100\%, \tag{2}$$

$$\varphi_{app} = \frac{N_A \int_0^t \left(C_{NO,\,i} - C_{NO,\,f} \right) V_t}{\text{photon flux} \cdot \text{irradiation area} \cdot t \cdot 1000\,M} \cdot 100\%, \tag{3}$$

$$\alpha_{DeNOx} = \eta \left(1 - 3\gamma \right) C_{NO,\,i}, \tag{4}$$

where C_{NO} is the concentration of NO (ppb), C_{NO2} is the concentration of NO$_2$ (ppb), the index "i" represents the initial concentration, and the index "f" represents the final concentration. N_A is the Avogadro constant (mol^{-1}), V_t is the flow rate of NO (L·min^{-1}), and M is the molecular weight of NO (g·mol^{-1}). The photon flux in the photocatalytic experiment is 2.72·10^{19} cm^{-2}·min^{-1}, the irradiation area for the 12 cm diameter petri dish is 113.1 cm^2.

In addition, the bandgap energy of materials was calculated by using the Tauc and the Kubelka–Munk equation as described in Equations 5–7 [43]:

$$E = h\nu = \frac{hc}{\lambda}, \tag{5}$$

$$\left(\alpha h\nu \right)^r = B \left(h\nu - E_g \right), \tag{6}$$

$$\left(F(R) h\nu \right)^r = B \left(h\nu - E_g \right), \tag{7}$$

where E is the photon energy (eV), h is Planck's constant (4.132·10^{-15} eV·s), ν is the photon frequency (s^{-1}), c is the velocity of light (nm·s^{-1}), λ is the wavelength (nm), α is the absorption coefficient, B is a constant, and E_g is the bandgap energy (eV), R is the reflectance value.

Results and Discussion
Photocatalytic performance

The photocatalytic NO removal efficiency of the materials is shown in Figure 2a. The efficiency gradually increased during the first 5 min of the photocatalytic reaction and remains stable until the end of the photocatalytic reaction. The photocatalytic NO removal efficiency values are 0.6%, 62.8%, 16.8%, 68.4%, 75.4%, and 72.1% for the blank sample, g-C$_3$N$_4$, MgO, 1%
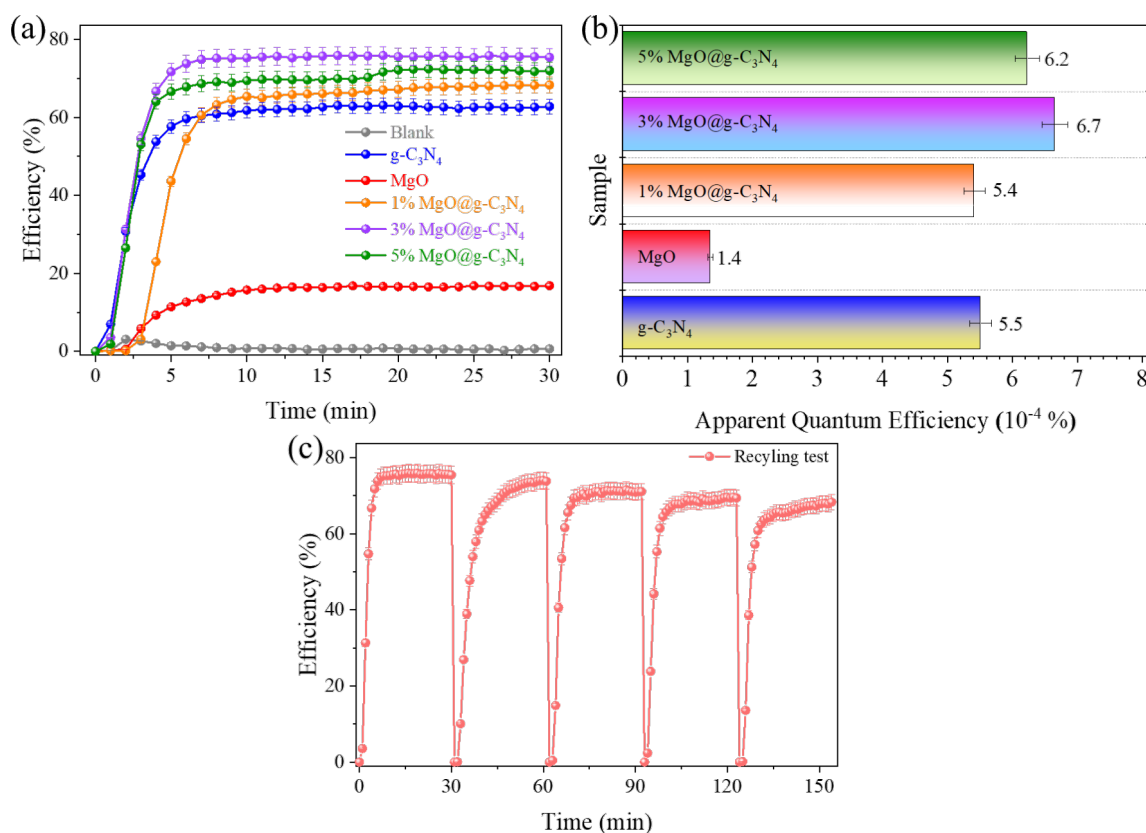
Figure 2: (a) Photocatalytic NO degradation efficiency, (b) apparent quantum efficiency of the materials, and (c) photocatalytic recycling test of 3% MgO@g-C$_3$N$_4$.

MgO@g-C$_3$N$_4$, 3% MgO@g-C$_3$N$_4$, and 5% MgO@g-C$_3$N$_4$, respectively. The photocatalytic NO removal efficiency is increased by combining MgO with g-C$_3$N$_4$. The results indicate that MgO@g-C$_3$N$_4$ heterojunction structures have been successfully synthesized with high photocatalytic NO degradation efficiency under visible light by one-step pyrolysis (see Table 1 for a comparison of the photocatalytic NO removal efficiency values). Also, the AQE has been calculated according to Equation 3. The AQE values (10^{-4}%) of g-C$_3$N$_4$, MgO, 1% MgO@g-C$_3$N$_4$, 3% MgO@g-C$_3$N$_4$, and 5% MgO@g-C$_3$N$_4$ are 5.5, 1.4, 5.4, 6.7, and 6.2, respectively. The AQE results show (Figure 2b) that photons are most efficient in 3% MgO@g-C$_3$N$_4$. The heterojunction structure has enhanced the photocatalytic activities of the materials [44]. In addition, the photocatalytic reusability of 3% MgO@g-C$_3$N$_4$ was shown by a five-cycle recycling test under identical experimental conditions (Figure 2c). The photocatalytic NO degradation efficiency in the recycling test is 75.4%, 73.8%, 71.1%, 69.4%, and 68.3% after five cycles, respectively. The photocatalytic NO

degradation efficiency decreased by 7% after five cycles. The FTIR spectra and the XRD patterns of the 3% MgO@g-C$_3$N$_4$ before and after the recycling test are shown in Figure S1a and Figure S1b of Supporting Information File 1, respectively. The results indicate the high reusability of 3% MgO@g-C$_3$N$_4$ [45].

The conversion rates of NO to NO$_2$ and by-products have been calculated (Figure 3a). The conversion rates of NO to NO$_2$ of g-C$_3$N$_4$, MgO, 1% MgO@g-C$_3$N$_4$, 3% MgO@g-C$_3$N$_4$, and 5% MgO@g-C$_3$N$_4$ are 34.6%, 9.6%, 34.9%, 21.9%, and 25.8%, respectively. Besides, the rates of converting NO to by-products of g-C$_3$N$_4$, MgO, 1% MgO@g-C$_3$N$_4$, 3% MgO@g-C$_3$N$_4$, and 5% MgO@g-C$_3$N$_4$ are 28.2%, 7.3%, 34.4%, 53.5%, and 46.3%, respectively. In this study, the by-products are defined as any nitrogen species (e.g., N$_2$O$_5$, N$_2$O, and NO$_3^-$) except NO$_2$, which are unstable and can be absorbed by plants [46]. MgO generates the lowest amount of NO$_2$ and by-products due to the lowest photocatalytic NO removal efficiency (16.8%). 3% MgO@g-C$_3$N$_4$ has the lowest NO$_2$ (21.9%) and highest

Table 1: Comparison of photocatalytic NO removal of current photocatalyst systems under visible light.

Material	Initial NO concentration (ppb)	Light source	Irradiation time (min)	Dosage (g)	Flowrate (L·min^{-1})	NO removal efficiency (%)	NO$_2$ generation	Ref.
BiOIO$_3$/ g-C$_3$N$_4$	600	xenon 300 W	30	0.1	1.2	57	80 (ppb)	[72]
SnO$_2$/ g-C$_3$N$_4$	600	tungsten halogen 150 W	30	0.4	N/A	32	6%	[73]
Ti$_3$C$_2$@TiO$_2$/ g-C$_3$N$_4$	430	xenon- 300 W	30	N/A	N/A	29	18.7 (ppb)	[74]
rGO/ Fe-doped g-C$_3$N$_4$	1000	metal halide 250 W	30	N/A	N/A	93.4	N/A	[75]
FAPbBr$_3$/g-C$_3$N$_4$	600	xenon	60	0.1	1.2	58	0.3 (ppb)	[76]
g-C$_3$N$_4$/SnO$_2$	500	xenon- 300 W	30	0.2	0.6	35	2%	[77]
TiO$_2$@g-C$_3$N$_4$	500	xenon- 300 W	30	0.2	0.5	90.2	5.3%	[44]
g-C$_3$N$_4$@BiOCl/ Bi$_{12}$O$_{17}$Cl$_2$	500	tungsten halogen 100 W	30	0.2	1	46.8	N/A	[78]
MoS$_2$/g-C$_3$N$_4$	600	tungsten halogen 150 W	30	0.2	N/A	51.7	N/A	[79]
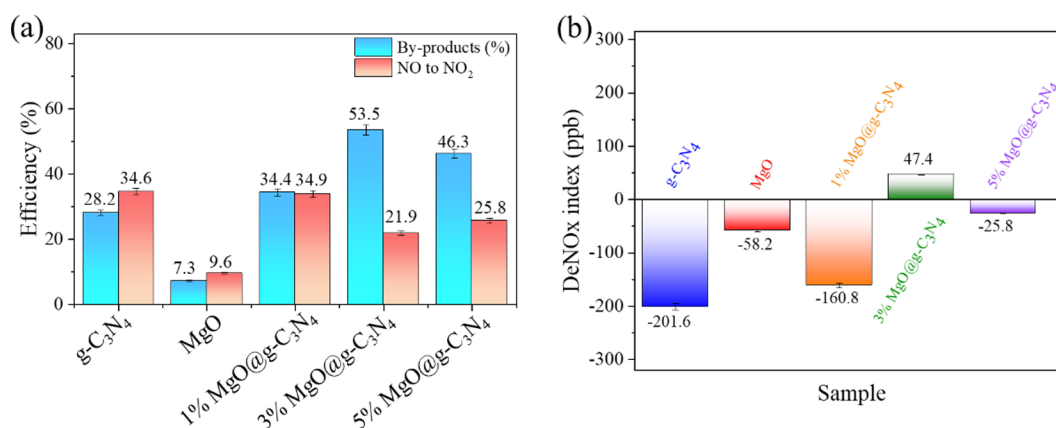
Figure 3: (a) NO conversion and (b) DeNOx index of the materials.

by-product (53.5%) generation. In addition, the NO$_2$ generation of g-C$_3$N$_4$ is almost equal to that of 1% MgO@g-C$_3$N$_4$. This can be explained by the low amount of MgO (only 1%). 3% MgO@g-C$_3$N$_4$ shows the highest photocatalytic NO removal efficiency with the lowest NO$_2$ generation, which indicates a possible future application of 3% MgO@g-C$_3$N$_4$. Also, the DeNOx index values have been calculated according to Equa-

tion 4 [47]. The values of g-C$_3$N$_4$, MgO, 1% MgO@g-C$_3$N$_4$, 3% MgO@g-C$_3$N$_4$, and 5% MgO@g-C$_3$N$_4$ are −201.6%, −58.2%, −160.8%, 47.4%, and −25.8%, respectively.

XRD and FTIR analyses

XRD patterns of the synthesized materials are shown in Figure 4a. There are two distinct diffraction peaks at 2θ = 13°

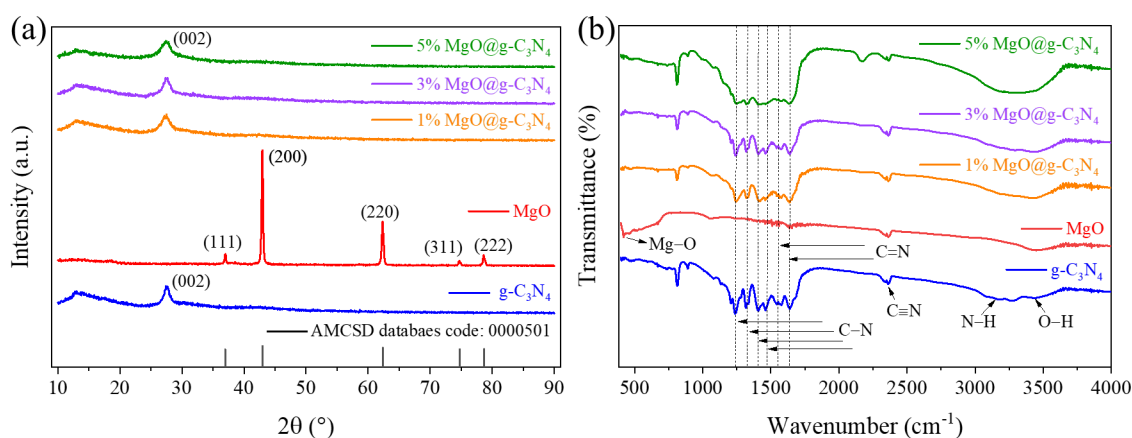**Figure 4:** (a) XRD patterns and (b) FTIR spectra of the materials.

and 27.4°, which were assigned to the (100) and (002) planes of g-C_3N_4, respectively [48]. Diffraction peaks of the pure MgO sample are detected at 36.9°, 42.9°, 62.5°, 74.8°, and 78.7°, which were attributed to the (111), (200), (220), (311), and (222) planes, respectively [AMCS: 000501] [49,50]. All MgO@g-C_3N_4 samples show the characteristic peaks of g-C_3N_4. No impurities are detected in the MgO@g-C_3N_4 samples. There are no reflections of MgO in all MgO@g-C_3N_4 samples, due to the low amount of MgO in the MgO@g-C_3N_4 samples. This agrees with previous studies, in which characteristic peaks of MgO were only detected when MgO amounts higher than 5% had been added [33,51].

Figure 4b shows the FTIR spectra of g-C_3N_4, MgO, and MgO@g-C_3N_4. For pure g-C_3N_4, the broad peak in the range of 3000–3600 cm^{-1} was attributed to the stretching vibrations of N–H and O–H bonds, indicating the existence of amino groups and adsorbed water molecules in the material [32,52]. The characteristic peaks at 1240, 1320, 1407, and 1465 cm^{-1} were associated with the stretching vibrations of aromatic C–N bonds, and the typical peaks at 1562 and 1642 cm^{-1} characterize the presence of C=O bonds [53,54]. In addition, the characteristic peak at 810 cm^{-1} matches with the typical breathing mode of triazine. After adding MgO, the distinct peaks of all MgO@g-C_3N_4 heterojunctions are similar to that of pure g-C_3N_4, indicating that the crystal structure of g-C_3N_4 remains unchanged. In addition, the small peak at 419 cm^{-1} proves the presence of MgO in MgO@g-C_3N_4 [55].

SEM and TEM analyses

The morphology of g-C_3N_4, MgO, and 3%MgO@g-C_3N_4 has been determined through SEM and TEM analyses. The typical

bulk structure of g-C_3N_4 is shown in Figure 5e,f. The difference between the morphologies of MgO and g-C_3N_4 is difficult to observe by SEM (Figure 5c,d). Figure 5a and Figure 5b show that the morphology of 3%MgO@ g-C_3N_4 is similar to that of pure g-C_3N_4. The results indicate that the morphology of 3% MgO@g-C_3N_4 is identical to that of g-C_3N_4 because the added amount of MgO is very low, as determined by EDS mapping. The EDS mapping images of 3% MgO@g-C_3N_4 are shown in Figure 6 and Figure S2 (Supporting Information File 1). The weight percentages of C, N, Mg, and O are 37, 52, 9, and 2 wt %, respectively. The weight fractions of Mg and O are the lowest, indicating that the amount of MgO in the MgO@g-C_3N_4 sample is too low. The shape of g-C_3N_4 is easy to observe in Figure 7c,d. However, the shape of MgO is complicated to determine by TEM and HR-TEM (Figure 7a,b). These results prove the presence of MgO in the compound.

Chemical state analysis

XPS and HR-XPS have been employed to determine the chemical states of the materials. XPS survey scans of g-C_3N_4 MgO and 3% MgO@ g-C_3N_4 are shown in Figure 8a. The peaks at 87 and 530 eV were assigned to the Mg 2s and O 1s levels of MgO, respectively. The peaks at 287 and 397 eV were assigned to the C 1s and N 1s levels of g-C_3N_4, respectively [12,56,57]. In the MgO sample, the peaks of Mg 2p, Mg KLL, O loss, and O KLL levels are observed at 46, 304, 555, and 978 eV, respectively [58,59]. The HR-XPS of the C 1s level are shown in Figure 8b. The peak at 283 eV was assigned to the C–C coordination in MgO, and the peak at 287 eV was assigned to N–C=N bonds of g-C_3N_4. The latter peak only appears in g-C_3N_4 and 3% MgO@g-C_3N_4. However, the former peak of MgO and g-C_3N_4 occurs only in 3% MgO@g-C_3N_4. The C 1s peaks of
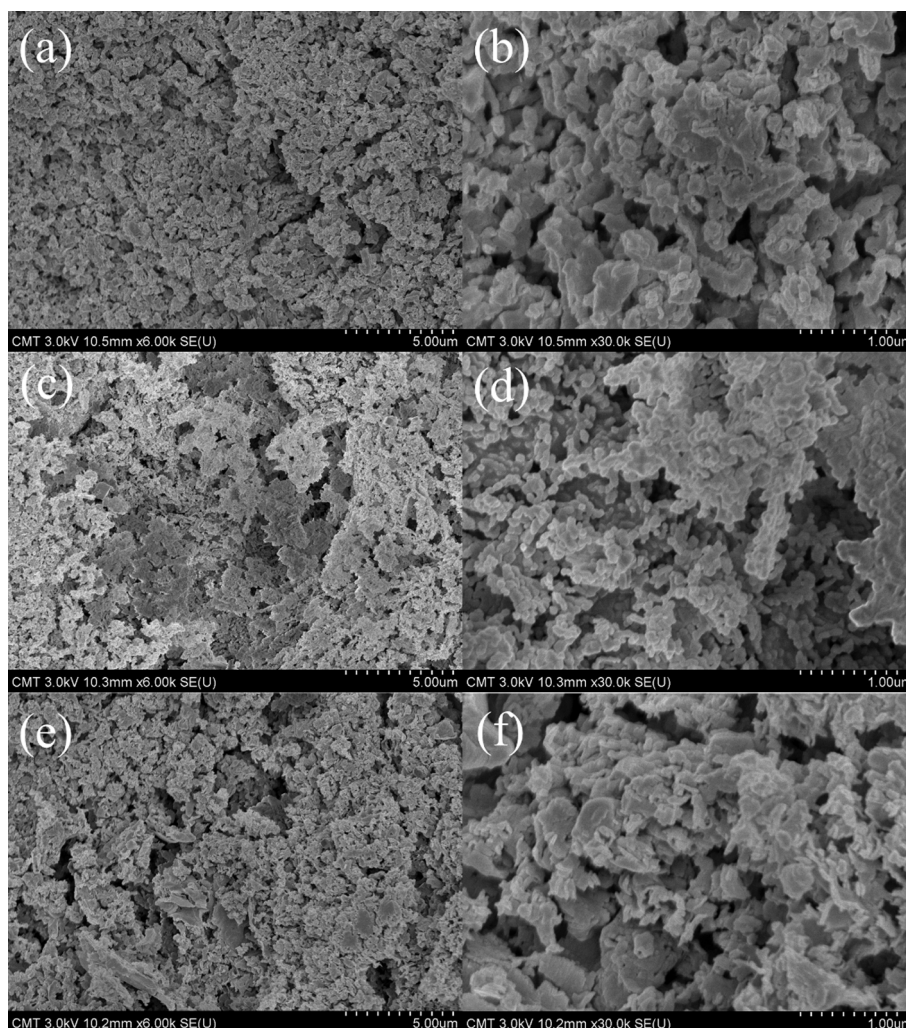
Figure 5: SEM images of (a, b) 3%MgO@g-C$_3$N$_4$, (c, d) MgO, and (e, f) g-C$_3$N$_4$.

the materials do not change during the pyrolysis. The HR-XPS of the N 1s level of the materials is shown in Figure 8c. The peaks at 397 and 399 eV correspond to the C–N=C bonds and the N–(C)$_3$ structures of g-C$_3$N$_4$, respectively [60]. Figure 8d shows the peak of Mg–O bonds in MgO at 398 eV [61]. The Mg 2s peaks of MgO are shown in Figure 8e and Figure 8f. The peaks at 87 eV (Figure 8e) and 88 eV (Figure 8f) confirm the metallic state of Mg [62]. The peaks of the O 1s and Mg 2s levels in 3% MgO@g-C$_3$N$_4$ are too weak.

Optical properties

DRS spectra have been measured to understand the optical absorption characteristics of the materials (Figure 9). The g-C$_3$N$_4$ sample significantly absorbs light at a peak around 440 nm, corresponding to the direct and the indirect bandgap of 2.83

and 2.68 eV, respectively (Figure 9b,d). MgO with a wide bandgap shows absorption below 400 nm in both Kubelka–Munk and Tauc plots (Figure 9a,c). After adding MgO to g-C$_3$N$_4$, the absorption of the MgO@ g-C$_3$N$_4$ samples slightly shifts to the visible light region. The optical direct and indirect bandgap energy is slightly reduced, corresponding to the increase in MgO fraction. The indirect bandgap energies of 1% MgO@g-C$_3$N$_4$, 3% MgO@g-C$_3$N$_4$, and 5% MgO@g-C$_3$N$_4$ are 2.79, 2.73, and 2.69 eV, respectively. The trend of the direct bandgap is the same. The bandgap of the materials reduces with increasing amounts of added MgO. The bandgap reduction can be attributed to Mg−N bonds in the MgO@g-C$_3$N$_4$ materials, which promote charge transport, thus, increasing the photocatalytic efficiency [33,51]. Generally, smaller bandgaps lead to better light absorption, indicating the high photocatalytic activi-
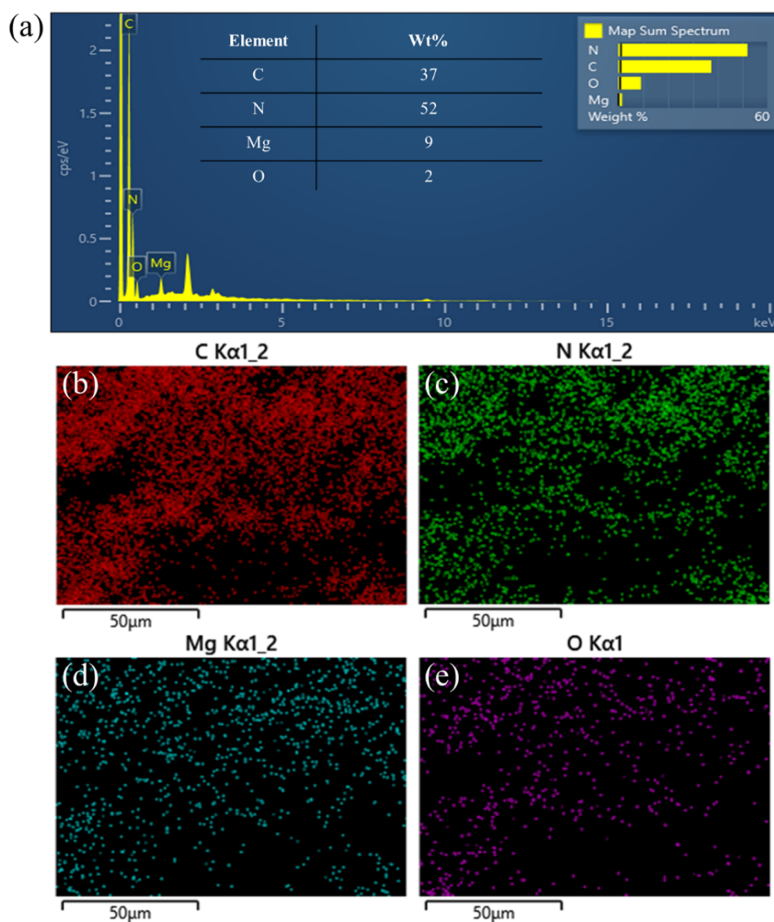
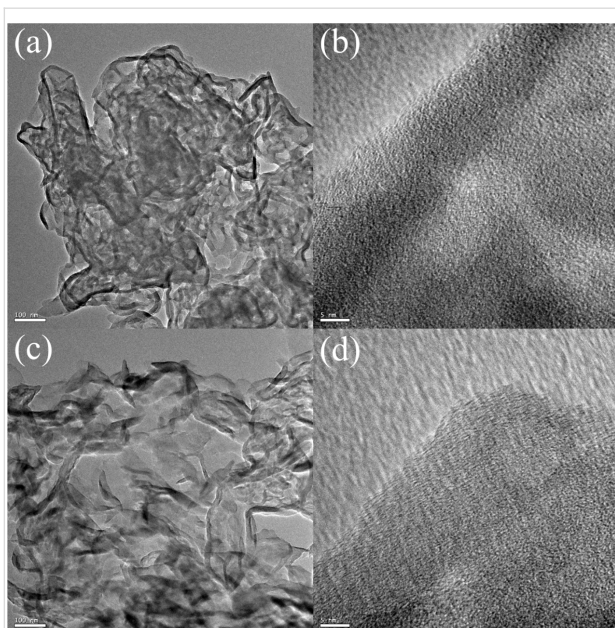**Figure 6:** (a) Elemental composition and (b–e) EDS mappings of 3% MgO@g-C$_3$N$_4$.

Figure 7: TEM and HR–TEM images of (a, b) MgO@g-C$_3$N$_4$ and (c, d) g-C$_3$N$_4$.

ty of MgO@g-C$_3$N$_4$ under visible light and also the existence of MgO in the MgO@g-C$_3$N$_4$ heterojunction materials. However, with a smaller bandgap, the recombination of e$^-$–h$^+$ pairs will be faster, which decreases the photocatalytic activity of the materials [63]. As shown in Figure 9a and Figure 9c, the materials mostly absorb in the UV range (200–400 nm), with a sudden decrease in the visible range. The absorbance of 3% MgO@g-C$_3$N$_4$ is more substantial than the absorbance of 1% MgO@g-C$_3$N$_4$ and 5% MgO@g-C$_3$N$_4$ in the UV and visible ranges. These results indicate that the higher photocatalytic NO removal efficiency of the 3% MgO@g-C$_3$N$_4$ strongly depends on the optical properties.

Photoluminescence

Fluorescence spectra of MgO and 3% MgO@g-C$_3$N$_4$ are shown in Figure 10a and Figure 10b, respectively. MgO shows strong fluorescence at 270 nm with an excitation wavelength (270 nm) in the UV range. MgO also shows another emission wavelength at 380 nm with an excitation wavelength (770 nm) in the visible range, which could be caused by the native structural defects in MgO [18]. 3% MgO@g-C$_3$N$_4$ shows intense fluores-
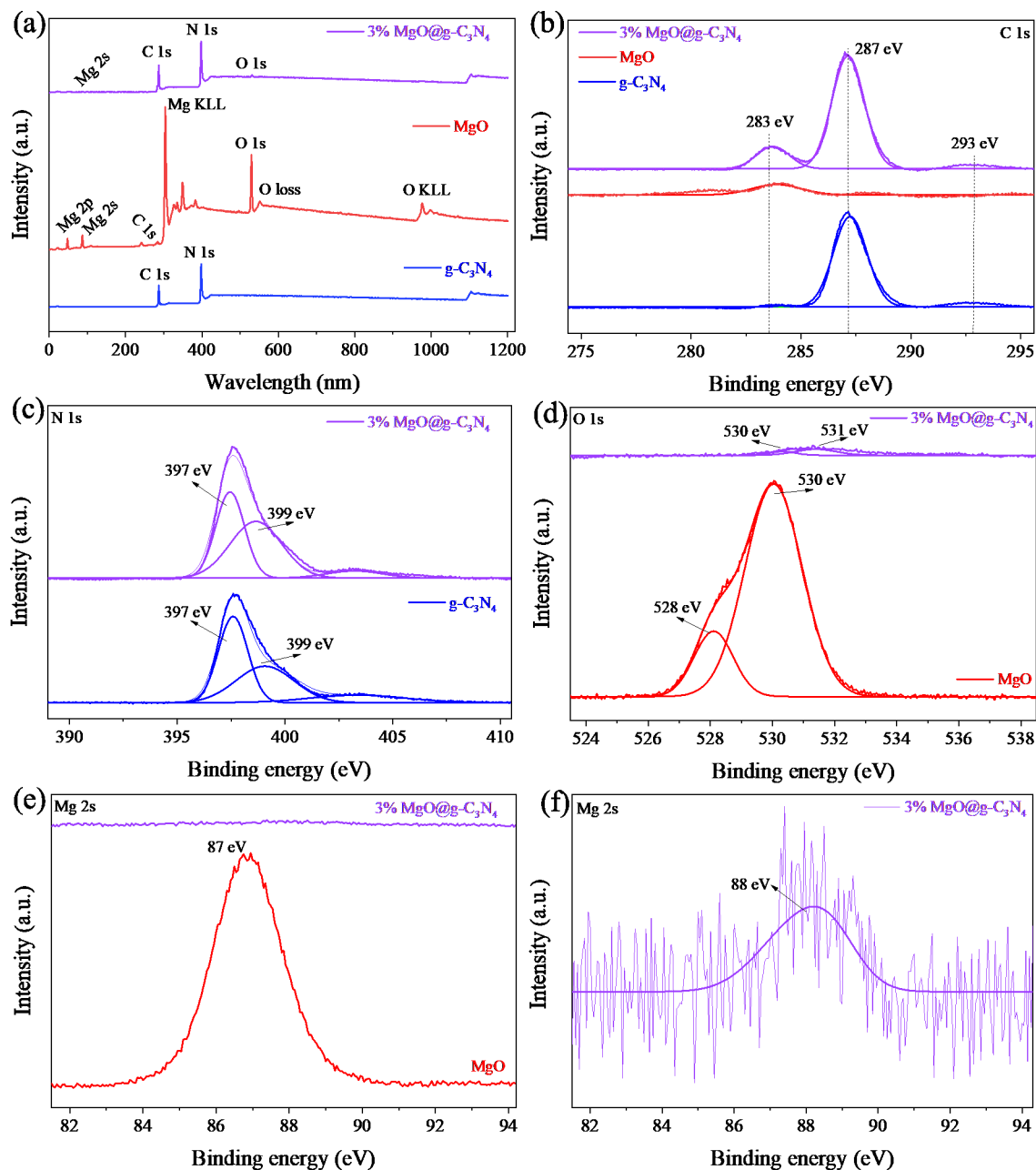
Figure 8: The XPS survey (a), HR–XPS C1s (b), N 1s (c), O 1s (d), C 1s (c), and Mg 2s (e, f) of the materials.

cence at 420 nm via excitation at 850 nm, due to the recombination of charge carriers. The photogenerated electrons from the valance band (VB) of g-C_3N_4 migrate to the conduction band (CB). The excited electrons in the CB of g-C_3N_4 can then return to energy bands between the CB and VB of g-C_3N_4 to produce an emission with an energy of about 1.5 eV. The energy band in g-C_3N_4 can be attributed to transitions between C atoms and N atoms [64-66]. Also, Liang and co-workers reported that the recombination of the e⁻–h⁺ pairs could be inhibited by doping MgO into g-C_3N_4 [32]. When MgO is added, the defect concen-

tration increases and Mg and O vacancies are generated in MgO@g-C_3N_4. These defects work as the electron traps, which enhance the capacity to separate photogenerated e⁻–h pairs in MgO@g-C_3N_4. The photogenerated e⁻–h⁺ pairs in the defects also contribute to the photocatalytic reaction [67,68].

Photocatalytic mechanism

Trapping experiments were carried out to evaluate the involvement of electrons, holes, and reactive oxygen species. The used trapping agents were KI (h⁺), $K_2Cr_2O_7$ (e⁻), and IPA (•OH).
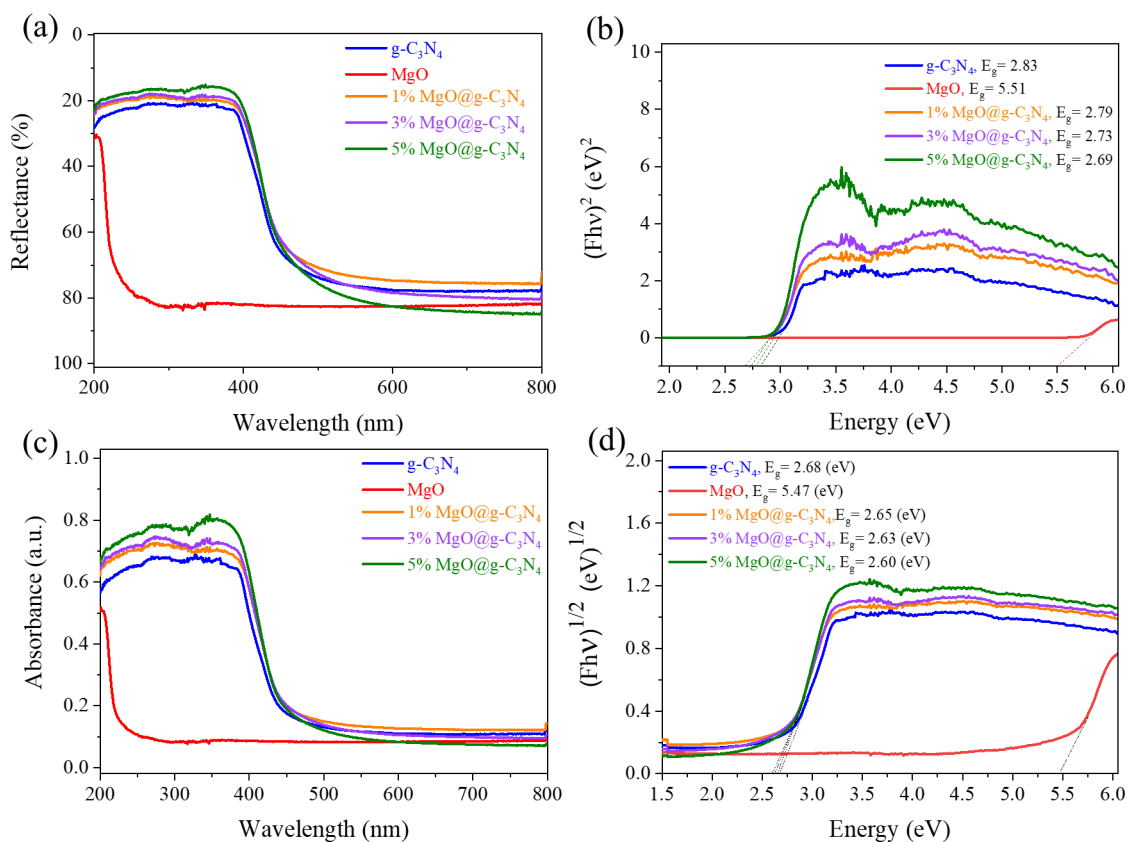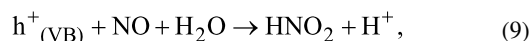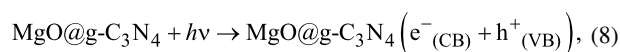
Figure 9: (a) DRS reflectance spectra, (b) direct bandgap, (c) DRS absorbance spectra, and (d) indirect bandgap of the materials.

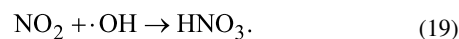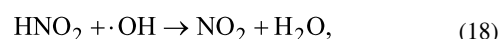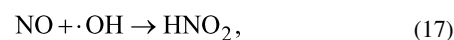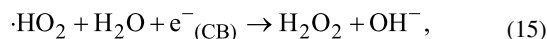Figure 11a shows the reduction in efficiency when different scavengers are present. The photocatalytic NO degradation efficiency decreases significantly from 75.4% to 36.4% in the presence of KI. $K_2Cr_2O_7$ as electron scavenger also reduces the NO decomposition by about 1.3 times. The weak contribution of •OH radicals in the NO degradation is clearly shown, with a reduction in efficiency by only about 1%. Hence, electrons and holes are the main contributors to the photocatalytic NO degradation.
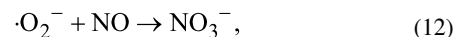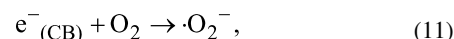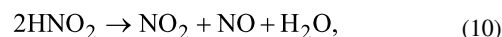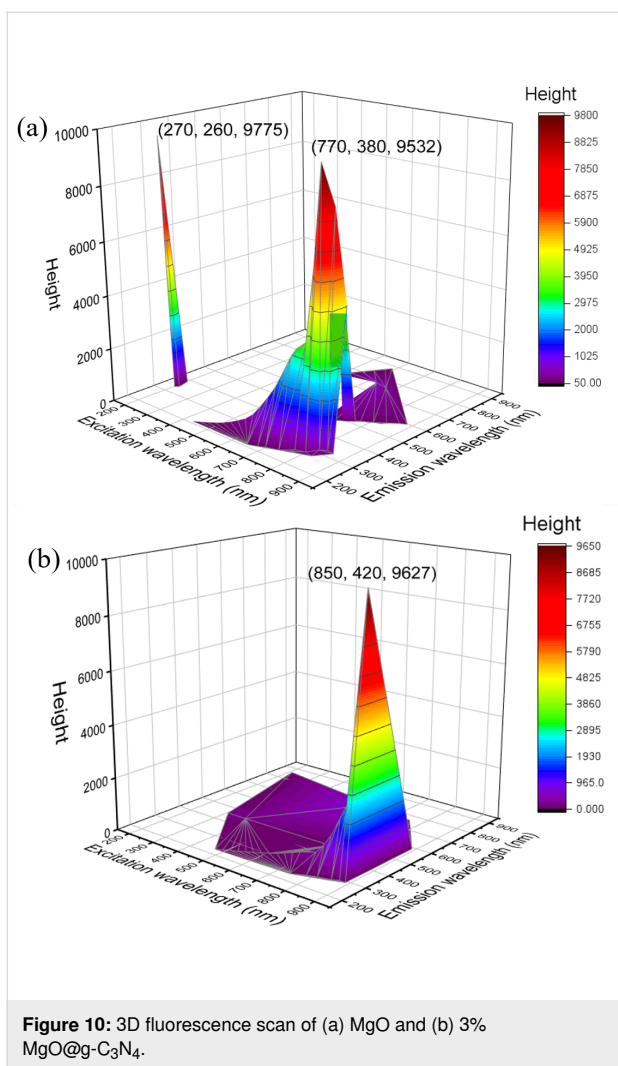
Also, ESR was used to determine accurately the reaction mechanism of the material. Figure 11b shows that under visible light and using DMPO–H_2O and DMPO–OH, the material generates •OH and •O_2 radicals. In contrast, only •OH radicals are generated in the dark, but to a very low extent. Hence, the generation of •O_2 radicals contributes significantly to the photocatalytic NO degradation efficiency.

A photocatalysis mechanism of MgO@g-C_3N_4 is proposed taking into account the results of the DRS and ESR analyses and trapping tests. Because of the large bandgap of MgO, only
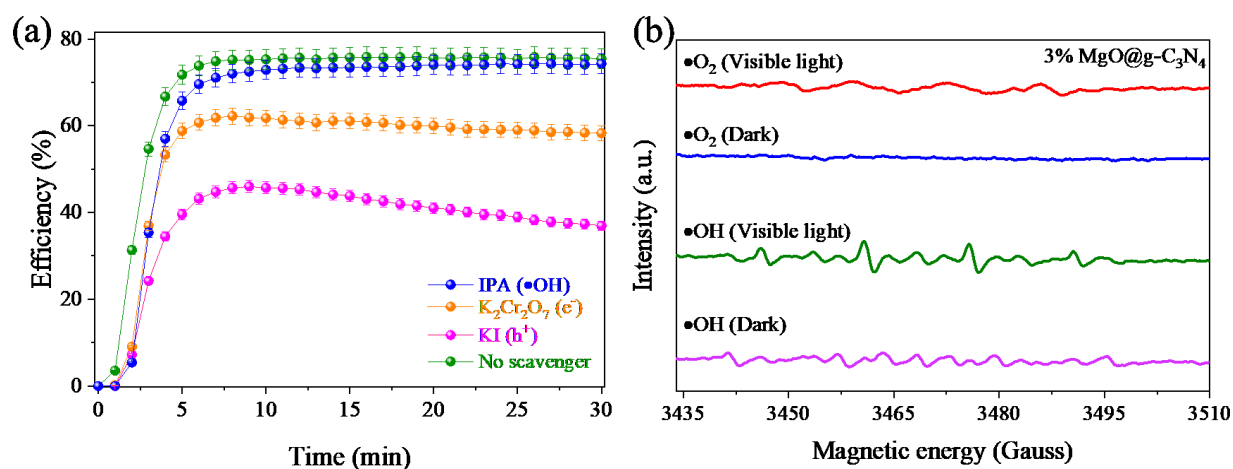
g-C_3N_4 generates e^-–h^+ pairs under visible light (Equation 8). The holes can degrade NO directly by oxidizing NO into NO_2 (Equations 9 and 10) [47,69]. Simultaneously, at the CB of g-C_3N_4, electrons are excited and react with O_2 to produce •O_2^- radicals. In addition, these electrons also migrate across the CB of MgO, creating excess electrons in MgO and avoiding the recombination at g-C_3N_4. Then, the photogenerated electrons react with O_2 to produce •O_2^- radicals (Equation 11). These •O_2^- radicals decompose NO to NO_3 and prevent the formation of NO_2 (Equation 12). Also, •O_2^- reacts with H_2O to produce •HO_2 radicals and OH^- (Equation 13). Then, the •HO_2 decomposes NO to form NO_2 and •OH (Equation 14). Also, •HO_2 also reacts with H_2O and electrons to produce H_2O_2 (Equation 15). Finally, H_2O_2 generates two •OH radicals to decompose NO (Equations 16–19) [70,71].

$$MgO@g\text{-}C_3N_4 + h\nu \rightarrow MgO@g\text{-}C_3N_4 \left(e^-_{(CB)} + h^+_{(VB)} \right), \quad (8)$$

$$h^+_{(VB)} + NO + H_2O \rightarrow HNO_2 + H^+, \quad (9)$$

$$2HNO_2 \rightarrow NO_2 + NO + H_2O, \qquad (10)$$

$$e^-_{(CB)} + O_2 \rightarrow \cdot O_2^-, \qquad (11)$$

$$\cdot O_2^- + NO \rightarrow NO_3^-, \qquad (12)$$

$$\cdot O_2^- + H_2O \rightarrow \cdot HO_2 + OH^-, \qquad (13)$$

$$NO + \cdot HO_2 \rightarrow NO_2 + \cdot OH, \qquad (14)$$

$$\cdot HO_2 + H_2O + e^-_{(CB)} \rightarrow H_2O_2 + OH^-, \qquad (15)$$

$$H_2O_2 \rightarrow 2 \cdot OH, \qquad (16)$$

$$NO + \cdot OH \rightarrow HNO_2, \qquad (17)$$

$$HNO_2 + \cdot OH \rightarrow NO_2 + H_2O, \qquad (18)$$

$$NO_2 + \cdot OH \rightarrow HNO_3. \qquad (19)$$
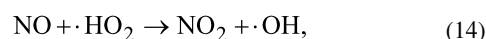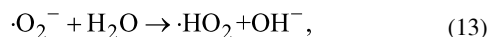
Conclusion

MgO@g-C$_3$N$_4$ heterojunction materials were effectively synthesized by one-step pyrolysis of commercial MgO and urea. The photocatalytic efficiencies of the synthesized materials were increased dramatically by mixing MgO and g-C$_3$N$_4$. 3% MgO@g-C$_3$N$_4$ possessed the highest photocatalytic NO removal efficiency, reaching 75.4%. In addition, the photocatalytic NO removal efficiency of the MgO@g-C$_3$N$_4$ heterojunction materials was decreased when the amount of MgO exceeded 3%. An enhanced apparent quantum efficiency of (6.7×10^{-4})% as well as an extended lifetime of photogener-

Figure 10: 3D fluorescence scan of (a) MgO and (b) 3% MgO@g-C$_3$N$_4$.

Figure 11: (a) Trapping test results of the materials and (b) detection of radicals over over 3% MgO@g-C$_3$N$_4$ by ESR.

ated electrons based on the heterojunction structure were obtained by combining MgO and g-C$_3$N$_4$. Moreover, the conversion rates of NO to NO$_2$ and by-products of the 3% MgO@g-C$_3$N$_4$ were the lowest (21.9%) and the highest (53.5%), respectively. Also, 3% MgO@ g-C$_3$N$_4$ showed high reusability after a five-cycle recycling test, when the photocatalytic NO removal efficiency decreased only by 7.1%. The results indicated that 3% MgO@g-C$_3$N$_4$ could be applied in the future as an excellent photocatalyst with high removal efficiency and low generation of toxic products. FTIR, XPS, and EDS measurements were carried out to confirm the presence of MgO in the MgO@g-C$_3$N$_4$ heterojunctions. Although MgO was difficult to determine in the MgO@g-C$_3$N$_4$ heterojunctions, the addition of MgO affected the optical properties of the MgO@g-C$_3$N$_4$ heterojunctions. The DRS result showed that the bandgap of the MgO@g-C$_3$N$_4$ heterojunctions decreased by adding larger amounts of MgO. The light absorption of 3% MgO@g-C$_3$N$_4$ was higher than that of 1% MgO@g-C$_3$N$_4$ and 5% MgO@g-C$_3$N$_4$ in the visible and UV range, which increased the photocatalytic performance under visible light irradiation. The PL results confirmed the presence of vacancies in the MgO@g-C$_3$N$_4$ heterojunctions. MgO@g-C$_3$N$_4$ is promising for large-scale fabrication via this simple and fast method. This study provides a new way to synthesize a MgO@g-C$_3$N$_4$ heterojunction materials and an understanding of the photocatalytic mechanism of the MgO@g-C$_3$N$_4$ heterojunction applied in the removal of NO.

Supporting Information

Supporting Information File 1
Additional figures.
[https://www.beilstein-journals.org/bjnano/content/supplementary/2190-4286-13-96-S1.pdf]

ORCID® iDs
Minh-Thuan Pham - https://orcid.org/0000-0002-6069-445X
Duyen P. H. Tran - https://orcid.org/0000-0003-3152-7270
Xuan-Thanh Bui - https://orcid.org/0000-0003-1413-4985
Sheng-Jie You - https://orcid.org/0000-0003-0532-9916

Preprint

References

1. Van Viet, P.; Hoang The Vinh, T.; Thi Ngoc Dung, N.; Minh Thi, C. *Chem. Phys. Lett.* **2021,** *775,* 138642. doi:10.1016/j.cplett.2021.138642
2. Zhou, S.; Young, C. J.; VandenBoer, T. C.; Kahan, T. F. *Environ. Sci.: Processes Impacts* **2019,** *21,* 1374–1383. doi:10.1039/c9em00129h
3. Pham, M.-T.; Hussain, A.; Bui, D.-P.; Nguyen, T.-M. T.; You, S.-J.; Wang, Y.-F. *Environ. Technol. Innovation* **2021,** *23,* 101755. doi:10.1016/j.eti.2021.101755
4. Nguyen, V.-H.; Nguyen, B.-S.; Huang, C.-W.; Le, T.-T.; Nguyen, C. C.; Nhi Le, T. T.; Heo, D.; Ly, Q. V.; Trinh, Q. T.; Shokouhimehr, M.; Xia, C.; Lam, S. S.; Vo, D.-V. N.; Kim, S. Y.; Le, Q. V. *J. Cleaner Prod.* **2020,** *270,* 121912. doi:10.1016/j.jclepro.2020.121912
5. Asghar, U.; Rafiq, S.; Anwar, A.; Iqbal, T.; Ahmed, A.; Jamil, F.; Khurram, M. S.; Akbar, M. M.; Farooq, A.; Shah, N. S.; Park, Y.-K. *J. Environ. Chem. Eng.* **2021,** *9,* 106064. doi:10.1016/j.jece.2021.106064
6. Qie, F.; Zhu, J.; Rong, J.; Zong, B. *Bioresour. Technol.* **2019,** *292,* 122037. doi:10.1016/j.biortech.2019.122037
7. Wang, S.; Xu, S.; Gao, S.; Xiao, P.; Jiang, M.; Zhao, H.; Huang, B.; Liu, L.; Niu, H.; Wang, J.; Guo, D. *Sci. Rep.* **2021,** *11,* 11003. doi:10.1038/s41598-021-90532-9
8. Chen, R.; Zhang, T.; Guo, Y.; Wang, J.; Wei, J.; Yu, Q. *Chem. Eng. J.* **2021,** *420,* 127588. doi:10.1016/j.cej.2020.127588
9. Talebizadeh, P.; Babaie, M.; Brown, R.; Rahimzadeh, H.; Ristovski, Z.; Arai, M. *Renewable Sustainable Energy Rev.* **2014,** *40,* 886–901. doi:10.1016/j.rser.2014.07.194
10. He, F.; Jeon, W.; Choi, W. *Nat. Commun.* **2021,** *12,* 2528. doi:10.1038/s41467-021-22839-0
11. Wang, S.; Li, C.; Wang, T.; Zhang, P.; Li, A.; Gong, J. *J. Mater. Chem. A* **2014,** *2,* 2885–2890. doi:10.1039/c3ta14576j
12. Papailias, I.; Todorova, N.; Giannakopoulou, T.; Karapati, S.; Boukos, N.; Dimotikali, D.; Trapalis, C. *Appl. Surf. Sci.* **2018,** *430,* 225–233. doi:10.1016/j.apsusc.2017.08.084
13. Van Pham, V.; Mai, D.-Q.; Bui, D.-P.; Van Man, T.; Zhu, B.; Zhang, L.; Sangkaworn, J.; Tantirungrotechai, J.; Reutrakul, V.; Cao, T. M. *Environ. Pollut.* **2021,** *286,* 117510. doi:10.1016/j.envpol.2021.117510
14. Hoang The Vinh, T.; Minh Thi, C.; Van Viet, P. *Mater. Lett.* **2020,** *281,* 128637. doi:10.1016/j.matlet.2020.128637
15. Zhao, G.-Q.; Zou, J.; Hu, J.; Long, X.; Jiao, F.-P. *Sep. Purif. Technol.* **2021,** *279,* 119769. doi:10.1016/j.seppur.2021.119769
16. Van, K. N.; Huu, H. T.; Nguyen Thi, V. N.; Le Thi, T. L.; Truong, D. H.; Truong, T. T.; Dao, N. N.; Vo, V.; Tran, D. L.; Vasseghian, Y. *Chemosphere* **2022,** *289,* 133120. doi:10.1016/j.chemosphere.2021.133120

17. Mousavi, M.; Habibi-Yangjeh, A.; Pouran, S. R.
    J. Mater. Sci.: Mater. Electron. **2018,** *29,* 1719–1747.
    doi:10.1007/s10854-017-8166-x

18. Madona, J.; Sridevi, C. *Inorg. Chem. Commun.* **2022,** *138,* 109265.
    doi:10.1016/j.inoche.2022.109265

19. Huang, Z.; Zhao, X.; Xia, H.; Lu, F.; Hu, L.; Chu, P. K.
    J. Environ. Chem. Eng. **2021,** *9,* 105922.
    doi:10.1016/j.jece.2021.105922

20. Sharmin, F.; Chandra Roy, D.; Basith, M. A. *Int. J. Hydrogen Energy*
    2021, *46,* 38232–38246. doi:10.1016/j.ijhydene.2021.09.072

21. Qi, K.; Cheng, B.; Yu, J.; Ho, W. *J. Alloys Compd.* **2017,** *727,* 792–820.
    doi:10.1016/j.jallcom.2017.08.142

22. Murillo-Sierra, J. C.; Hernández-Ramírez, A.; Hinojosa-Reyes, L.;
    Guzmán-Mar, J. L. *Chem. Eng. J. Adv.* **2021,** *5,* 100070.
    doi:10.1016/j.ceja.2020.100070

23. Liu, D.; Kelly, T. L. *Nat. Photonics* **2014,** *8,* 133–138.
    doi:10.1038/nphoton.2013.342

24. Low, J.; Yu, J.; Jaroniec, M.; Wageh, S.; Al-Ghamdi, A. A.
    Adv. Mater. (Weinheim, Ger.) **2017,** *29,* 1601694.
    doi:10.1002/adma.201601694

25. Li, S.; Wang, C.; Cai, M.; Yang, F.; Liu, Y.; Chen, J.; Zhang, P.; Li, X.;
    Chen, X. *Chem. Eng. J.* **2022,** *428,* 131158.
    doi:10.1016/j.cej.2021.131158

26. Yu, H.; Jiang, L.; Wang, H.; Huang, B.; Yuan, X.; Huang, J.; Zhang, J.;
    Zeng, G. *Small* **2019,** 1901008. doi:10.1002/smll.201901008

27. Wang, C.; Cai, M.; Liu, Y.; Yang, F.; Zhang, H.; Liu, J.; Li, S.
    J. Colloid Interface Sci. **2022,** *605,* 727–740.
    doi:10.1016/j.jcis.2021.07.137

28. Wang, C.; Li, S.; Cai, M.; Yan, R.; Dong, K.; Zhang, J.; Liu, Y.
    J. Colloid Interface Sci. **2022,** *619,* 307–321.
    doi:10.1016/j.jcis.2022.03.075

29. Li, S.; Wang, C.; Liu, Y.; Cai, M.; Wang, Y.; Zhang, H.; Guo, Y.;
    Zhao, W.; Wang, Z.; Chen, X. *Chem. Eng. J.* **2022,** *429,* 132519.
    doi:10.1016/j.cej.2021.132519

30. Li, S.; Cai, M.; Wang, C.; Liu, Y.; Li, N.; Zhang, P.; Li, X.
    J. Mater. Sci. Technol. **2022,** *123,* 177–190.
    doi:10.1016/j.jmst.2022.02.012

31. Guo, M.; Zhou, Z.; Yan, S.; Zhou, P.; Miao, F.; Liang, S.; Wang, J.;
    Cui, X. *Sci. Rep.* **2020,** *10,* 18401. doi:10.1038/s41598-020-75003-x

32. An, W.; Tian, L.; Hu, J.; Liu, L.; Cui, W.; Liang, Y. *Appl. Surf. Sci.* **2020,**
    534, 147518. doi:10.1016/j.apsusc.2020.147518

33. Li, N.; Huang, M.; Zhou, J.; Liu, M.; Jing, D. *Chin. J. Catal.* **2021,** *42,*
    781–794. doi:10.1016/s1872-2067(20)63690-7

34. Ge, L.; Peng, Z.; Wang, W.; Tan, F.; Wang, X.; Su, B.; Qiao, X.;
    Wong, P. K. *J. Mater. Chem. A* **2018,** *6,* 16421–16429.
    doi:10.1039/c8ta05488f

35. Shelemanov, A. A.; Evstropiev, S. K.; Karavaeva, A. V.;
    Nikonorov, N. V.; Vasilyev, V. N.; Podruhin, Y. F.; Kiselev, V. M.
    Mater. Chem. Phys. **2022,** *276,* 125204.
    doi:10.1016/j.matchemphys.2021.125204

36. Panchal, P.; Paul, D. R.; Sharma, A.; Hooda, D.; Yadav, R.; Meena, P.;
    Nehra, S. P. *J. Photochem. Photobiol., A* **2019,** *385,* 112049.
    doi:10.1016/j.jphotochem.2019.112049

37. Dhiman, P.; Rana, G.; Kumar, A.; Sharma, G.; Vo, D.-V. N.;
    Naushad, M. *Environ. Chem. Lett.* **2022,** *20,* 1047–1081.
    doi:10.1007/s10311-021-01361-1

38. Chen, J.; Xiong, J.; Song, Y.; Yu, Y.; Wu, L. *Appl. Surf. Sci.* **2018,** *440,*
    1269–1276. doi:10.1016/j.apsusc.2018.01.228

39. Huang, Y.-C.; Chang, S.-Y.; Jehng, J.-M. *J. Phys. Chem. C* **2017,** *121,*
    19063–19068. doi:10.1021/acs.jpcc.7b05806

40. Vaizogullar, A. I. *Kinet. Catal.* **2018,** *59,* 418–427.
    doi:10.1134/s0023158418040146

41. Guerrand, H.; Pucheault, M.; Vaultier, M. Ionic Liquids. *Green Process
    Engineering;* CRC Press:: Boca Raton, FL, USA, 2015; pp 267–291.

42. Ohtani, B. *Adv. Inorg. Chem.* **2011,** *63,* 395–430.
    doi:10.1016/b978-0-12-385904-4.00001-9

43. Bui, D.-P.; Pham, M.-T.; Tran, H.-H.; Nguyen, T.-D.; Cao, T. M.;
    Pham, V. V. *ACS Omega* **2021,** *6,* 27379–27386.
    doi:10.1021/acsomega.1c04215

44. Pham, M.-T.; Luu, H. Q.; Nguyen, T.-M. T.; Tran, H.-H.; You, S.-J.;
    Wang, Y.-F. *Aerosol Air Qual. Res.* **2021,** *21,* 210276.
    doi:10.4209/aaqr.210276

45. Li, S.; Hu, S.; Jiang, W.; Zhang, J.; Xu, K.; Wang, Z.
    J. Colloid Interface Sci. **2019,** *556,* 335–344.
    doi:10.1016/j.jcis.2019.08.077

46. Roy, S.; Madras, G. *Curr. Org. Chem.* **2015,** *19,* 2122–2131.
    doi:10.2174/1385272819666150603235429

47. Pham, M.-T.; Tran, H.-H.; Nguyen, T.-M. T.; Bui, D.-P.; Huang, Y.;
    Cao, J.; You, S.-J.; Van Viet, P.; Nam, V. H.; Wang, Y.-F. *Acta Mater.*
    2021, *215,* 117068. doi:10.1016/j.actamat.2021.117068

48. Kumar, A.; Singh, S.; Khanuja, M. *Mater. Chem. Phys.* **2020,** *243,*
    122402. doi:10.1016/j.matchemphys.2019.122402

49. Xu, L.; Gao, S.; Chen, M.; Wu, Y.; Shinozaki, K. *Mater. Chem. Phys.*
    2020, *253,* 123368. doi:10.1016/j.matchemphys.2020.123368

50. Mohammed, W. M.; Yanilkin, I. V.; Gumarov, A. I.; Kiiamov, A. G.;
    Yusupov, R. V.; Tagirov, L. R. *Beilstein J. Nanotechnol.* **2020,** *11,*
    807–813. doi:10.3762/bjnano.11.65

51. Mao, N.; Jiang, J.-X. *Appl. Surf. Sci.* **2019,** *476,* 144–150.
    doi:10.1016/j.apsusc.2019.01.049

52. Yuan, Y.; Zhang, L.; Xing, J.; Utama, M. I. B.; Lu, X.; Du, K.; Li, Y.;
    Hu, X.; Wang, S.; Genç, A.; Dunin-Borkowski, R.; Arbiol, J.; Xiong, Q.
    Nanoscale **2015,** *7,* 12343–12350. doi:10.1039/c5nr02905h

53. Chen, Z.; Sun, P.; Fan, B.; Liu, Q.; Zhang, Z.; Fang, X. *Appl. Catal., B*
    2015, *170-171,* 10–16. doi:10.1016/j.apcatb.2015.01.024

54. Bojdys, M. J.; Müller, J.-O.; Antonietti, M.; Thomas, A. *Chem. – Eur. J.*
    2008, *14,* 8177–8182. doi:10.1002/chem.200800190

55. Dobrucka, R. *Iran. J. Sci. Technol.* **2018,** *42,* 547–555.
    doi:10.1007/s40995-016-0076-x

56. Li, D.; Xiao, Y.; Pu, M.; Zan, J.; Zuo, S.; Xu, H.; Xia, D.
    Mater. Chem. Phys. **2019,** *231,* 225–232.
    doi:10.1016/j.matchemphys.2019.04.016

57. Tan, L.; Xu, J.; Zhang, X.; Hang, Z.; Jia, Y.; Wang, S. *Appl. Surf. Sci.*
    2015, *356,* 447–453. doi:10.1016/j.apsusc.2015.08.078

58. Cimino, A. *Mater. Chem. Phys.* **1985,** *13,* 221–241.
    doi:10.1016/0254-0584(85)90057-4

59. Peng, Q.; Dai, Y.; Liu, K.; Luo, X.; He, D.; Tang, X.; Huang, G.
    J. Mater. Sci. **2020,** *55,* 11267–11283.
    doi:10.1007/s10853-020-04822-0

60. Wang, P.; Guan, Z.; Li, Q.; Yang, J. *J. Mater. Sci.* **2018,** *53,* 774–786.
    doi:10.1007/s10853-017-1540-5

61. Vesali-Kermani, E.; Habibi-Yangjeh, A.; Ghosh, S.
    J. Ind. Eng. Chem. (Amsterdam, Neth.) **2020,** *84,* 185–195.
    doi:10.1016/j.jiec.2019.12.033

62. Gu, W.; Lee, J. T.; Nitta, N.; Yushin, G. *Nanomater. Nanotechnol.*
    2014, *4,* 30. doi:10.5772/59931

63. Lenes, M.; Morana, M.; Brabec, C. J.; Blom, P. W. M.
    Adv. Funct. Mater. **2009,** *19,* 1106–1111. doi:10.1002/adfm.200801514

64. Wei, F.; Liu, Y.; Zhao, H.; Ren, X.; Liu, J.; Hasan, T.; Chen, L.; Li, Y.;
    Su, B.-L. *Nanoscale* **2018,** *10,* 4515–4522. doi:10.1039/c7nr09660g

65. Li, Y.; Gu, M.; Zhang, X.; Fan, J.; Lv, K.; Carabineiro, S. A. C.; Dong, F.
Mater. Today **2020,** *41,* 270–303. doi:10.1016/j.mattod.2020.09.004

66. Li, S.; Wang, C.; Liu, Y.; Xue, B.; Jiang, W.; Liu, Y.; Mo, L.; Chen, X.
Chem. Eng. J. **2021,** *415,* 128991. doi:10.1016/j.cej.2021.128991

67. Mageshwari, K.; Mali, S. S.; Sathyamoorthy, R.; Patil, P. S.
Powder Technol. **2013,** *249,* 456–462.
doi:10.1016/j.powtec.2013.09.016

68. Karthik, K.; Dhanuskodi, S.; Gobinath, C.; Prabukumar, S.;
Sivaramakrishnan, S. *J. Photochem. Photobiol., B* **2019,** *190,* 8–20.
doi:10.1016/j.jphotobiol.2018.11.001

69. Wang, J.; Yu, J.; Fu, Q.; Yang, H.; Tong, Q.; Hao, Z.; Ouyang, G.
ACS Cent. Sci. **2021,** *7,* 355–364. doi:10.1021/acscentsci.0c01600

70. Lasek, J.; Yu, Y.-H.; Wu, J. C. S. *J. Photochem. Photobiol., C* **2013,** *14,*
29–52. doi:10.1016/j.jphotochemrev.2012.08.002

71. Nikokavoura, A.; Trapalis, C. *Appl. Surf. Sci.* **2018,** *430,* 18–52.
doi:10.1016/j.apsusc.2017.08.192

72. Wang, B.; Chen, D.; Li, N.; Xu, Q.; Li, H.; He, J.; Lu, J.
J. Colloid Interface Sci. **2020,** *576,* 426–434.
doi:10.1016/j.jcis.2020.05.037

73. Zou, Y.; Xie, Y.; Yu, S.; Chen, L.; Cui, W.; Dong, F.; Zhou, Y.
Appl. Surf. Sci. **2019,** *496,* 143630. doi:10.1016/j.apsusc.2019.143630

74. Zhang, X.; Nie, J.; Rao, F.; Liu, H.; Wang, Y.; Qu, D.; Wu, W.;
Zhong, P.; Zhu, G. *Ceram. Int.* **2021,** *47,* 31302–31310.
doi:10.1016/j.ceramint.2021.08.003

75. Yang, X.; Cao, X.; Tang, B.; Shan, B.; Deng, M.; Liu, Y.
J. Photochem. Photobiol., A **2019,** *375,* 40–47.
doi:10.1016/j.jphotochem.2019.02.011

76. Xie, B.; Chen, D.; Li, N.; Xu, Q.; Li, H.; He, J.; Lu, J. *Chem. Eng. J.*
2022, *430,* 132968. doi:10.1016/j.cej.2021.132968

77. Van Viet, P.; Nguyen, H.-P.; Tran, H.-H.; Bui, D.-P.; Hai, L. V.;
Pham, M.-T.; You, S.-J.; Thi, C. M. *J. Sci.: Adv. Mater. Devices* **2021,**
6, 551–559. doi:10.1016/j.jsamd.2021.07.005

78. Zhang, W.; Liang, Y. *Front. Chem. (Lausanne, Switz.)* **2019,** *7,* 664.
doi:10.3389/fchem.2019.00664

79. Wen, M. Q.; Xiong, T.; Zang, Z. G.; Wei, W.; Tang, X. S.; Dong, F.
Opt. Express **2016,** *24,* 10205–10212. doi:10.1364/oe.24.010205